

Twist angle driven electronic structure evolution of twisted bilayer graphene

Jiawei Yu,^{1,2†} Guihao Jia,^{1,2†} Qian Li,^{1,2†} Yuyang Wang,^{1,2} Kebin Xiao,^{1,2} Yongkang Ju,³ Hongyun Zhang,^{1,2} Zhiqiang Hu,^{1,2} Yunkai Guo,^{1,2} Biao Lian,⁴ Peizhe Tang,³ Shuyun Zhou,^{1,2} Qi-Kun Xue,^{1,2,5,6*} and Wei Li^{1,2*}

¹*State Key Laboratory of Low-Dimensional Quantum Physics, Department of Physics, Tsinghua University, Beijing 100084, China*

²*Frontier Science Center for Quantum Information, Beijing 100084, China*

³*School of Materials Science and Engineering, Beihang University, Beijing 100191, China*

⁴*Department of Physics, Princeton University, Princeton, New Jersey 08544, USA*

⁵*Beijing Academy of Quantum Information Sciences, Beijing 100193, China*

⁶*Southern University of Science and Technology, Shenzhen 518055, China*

*To whom correspondence should be addressed: qkxue@mail.tsinghua.edu.cn; weili83@tsinghua.edu.cn

In twisted bilayer graphene (TBG) devices, local strains often coexist and entangle with the twist-angle dependent moiré superlattice, both of which can significantly affect the electronic properties of TBG. Here, using low-temperature scanning tunneling microscopy, we investigate the fine evolution of the electronic structures of a TBG device with continuous variation of twist angles from 0.32° to 1.29° , spanning the first (1.1°), second (0.5°) and third (0.3°) magic angles. We reveal the exotic behavior of the flat bands and remote bands in both the energy space and real space near the magic angles. Interestingly, we observe an anomalous spectral weight transfer between the two flat band peaks in the tunneling spectra when approaching the first magic angle, suggesting strong inter-flat-bands interactions. The position of the remote band peak can be an index for the twist angle in TBG, since it positively correlates with the twist angle but is insensitive to the strain. Moreover, influences of the twist angle gradient on symmetry breaking of the flat bands are also studied.

Because of its unique electronic structures with strong correlation and intriguing topology, magic-angle twisted bilayer graphene (MATBG) has attracted enormous attention¹⁻²⁷. As the twist angle is close to 1.1° (i.e., the first magic angle), the band structures of TBG are renormalized by the developed moiré superlattices between two graphene layers, and two flat bands (FBs) emerge¹⁻⁵. As the FBs are partially filled, the largely enhanced electronic correlation can give rise to novel phenomena, such as the correlated insulating phase⁴⁻⁹, unconventional superconductivity¹⁰⁻¹⁵, quantum anomalous Hall state¹⁶, and transition of

multiple topological phases¹⁷⁻²³. Recently, higher magic angles and moiré bands have also been studied²⁸.

Twist angle disorder^{3, 29, 30} and local strains^{5, 31-38} may form during the process of device fabrication. Strain can cause the broadening of the FBs and affect the electronic correlation^{33, 34}, and it may induce the inhomogeneity of twist angle as well. The twist angle gradient can generate intrinsic band bending²⁹. Therefore, electronic properties could be significantly different even in the devices with similar nominal twist angles³⁴⁻³⁶. On the other hand, we can also benefit from the imperfection of a device, since it can host continuously changing twist angles as well as the concomitant angle gradients. Such a device can therefore be an ideal platform to comprehensively investigate the electronic properties of TBG affected by strain and twist angle.

Scanning tunneling microscope/spectroscopy (STM/STS) captures the morphology of the moiré superlattice and measures the local electronic density of states (DOSs) of moiré bands, and thus is widely used to study TBG. For instance, sharp peaks in STS as the signature of FBs^{5-9, 39-42}, cascade electronic evolution between the FBs as a function of electron filling⁶, and the Chern insulating evolution of the partially filled FBs with magnetic field²³, have been observed in recent STM studies of MATBG.

In this study, by performing STM experiment on a specially-made TBG device, where the twist angles smoothly change from 0.32° to 1.29° , spanning the first (1.1°), second (0.5°) and third (0.3°) magic angles, we directly observe the evolution of the electronic structures of TBG as a function of twist angles on a single TBG device. A systematic evolution of the FBs as well as the remote bands with the twist angle in both the energy space and real space is revealed with atomic resolution. Interestingly, near the magic angle, an anomalous spectral weight transfer between the two FBs near the first magic angle is observed. Moreover, we investigate the effects of the twist angle gradient on the FBs, and find that the symmetry breaking of the two FBs has different response to the twist angle gradient.

Our TBG sample is stacked on a hexagonal boron nitride (hBN) substrate (see device schematic in Fig. 1a). The moiré pattern in TBG can be divided into three distinct regions based on the stacking configurations (see low right panel of Fig. 1a) between the top and bottom graphene layers: AA site, AB/BA domain, and DW (domain wall between AB and BA domains)³⁵.

Figure 1b is a STM topographic image of the TBG, showing an extensive flat area with deformed triangular moiré lattices (one triangular is denoted by red dashed line in Fig. 1b). Each vertex of the triangular lattice (the bright spot) corresponds to an AA site. The deformed moiré pattern here is consistent with the heterostrain-amplified moiré patterns in other strain-related works^{34, 35}. We focus on the region marked by an unclosed yellow dashed box in Fig. 1b, where several triangular lattices with continuously changing moiré wavelength are included. The area in the yellow dashed box is plotted in the left panel of Fig. 1c, and all AA sites are numbered and the red dashed lines mark the same triangular in Fig. 1b.

We measure the three wavelengths of moiré triangle: L_1 , L_2 , and L_3 (as defined in the left panel of Fig. 1c). The extracted values are summarized in the right panel of Fig. 1c, where the

wavelengths vary smoothly and continuously over the area. Based on the uniaxial heterostrain model^{7, 37}, we calculated the twist angle and strain of each moiré triangle. The twist angle varies continuously from 0.32° to 1.29° (see the right y-axis in Fig. 1c), and the calculated strain values are also schematically shown in Fig. 1c (see simulations in Fig. S2).

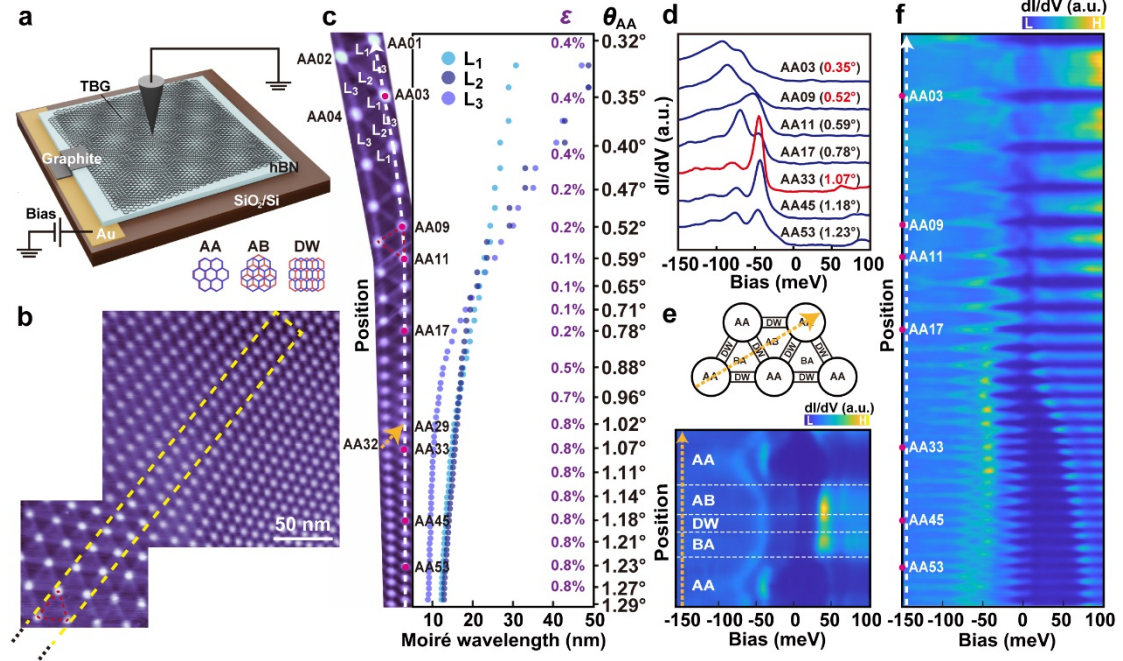


Fig. 1 | Evolution of tunneling spectra in a strained twisted bilayer graphene device with continuously changed twist angles spanning multiple magic angles. **a**, Sample schematic. TBG is stacked on hBN substrate and bias voltage V_b between the STM tip and TBG is applied through a graphite electrode. Three types of stacking configurations (AA, AB and DW) are shown on the bottom. **b**, STM topography of a large area on TBG spliced by two images ($200 \text{ nm} \times 200 \text{ nm}$ and $100 \text{ nm} \times 100 \text{ nm}$, bias voltage $V_b = -800 \text{ mV}$, tunneling current $I_t = 20 \text{ pA}$), the unclosed yellow dashed box marks the studied area, and the black dots represent the extended area (see Fig. S1 for the whole studied area). **c**, Moiré triangular wavelengths and their corresponding calculated twist angles. The left panel is the area within the yellow dashed box in **b**. The two red triangles in **b** and **c** correspond to the same location. L_1, L_2, L_3 are defined as the lengths of three sides of each moiré triangle, which are plotted in the right panel. The corresponding calculated twist angle and strain value of each moiré triangle are shown on the right y-axis. **d**, Tunneling spectra on the center of seven AA sites, marked by red dots in **c**. The magic angles are in red. **e**, dI/dV colormap taken along the orange dashed line in **c** across AA, AB, DW, BA and AA sites. The upper panel of **e** indicates the route of the dashed line in detail. **f**, dI/dV colormap taken along the arrowed white dashed line in **c**, in which the locations of the seven AA sites are also marked. Set point: **d-f**, $V_s = -200 \text{ mV}$, $I_t = 200 \text{ pA}$.

We present the tunneling spectra (or dI/dV spectra) of seven selected AA sites with their twist angles close to the first, second and third magic angles, respectively (Fig. 1d). Their corresponding locations are marked by red dots in Fig. 1c. The dI/dV spectra exhibit peak

features and higher DOSs in the energy range of around -90 meV to -30 meV, corresponding to the moiré FBs in TBG. The Fermi level (E_F) is far above the FBs, indicating that the FBs are fully occupied.

The spectrum taken on AA33, AA45, AA53 sites (Fig. 1d) show double peak features, corresponding to the two moiré FBs in TBG close to the first magic angle⁵. Spectra on the AA sites close to the second (AA09) and the third magic angles (AA03) show series of broad peaks, consistent with the multiple moiré FBs picture²⁸.

Figure 1e depicts the dI/dV colormap taken along the orange dashed line across AA32 to AA29 in Fig. 1c. It shows a detailed spatial evolution of DOSs along the route of AA-BA-DW-AB-AA near the first magic angle (see schematic in the upper panel of Fig. 1e). As the STM tip moves away from the center of the AA site, the two peaks of FBs shift towards E_F , showing a spatial evolution within the moiré triangle. Moreover, on the AB/BA domains and DWs, within the FBs' energy range, the DOSs are lower than that on the AA sites; while, at energies above E_F , DOSs are much higher, corresponding to the remote conduction bands (RCBs)⁶. Our results demonstrate that the electronic states from different energy bands in TBG are distributed at different locations: the FB electrons are mainly localized at the AA sites, while the RCB electrons are distributed elsewhere.

Figure 1f shows the dI/dV colormap taken along the arrowed white dashed line across AA sites and DWs. An oscillating electronic evolution of FBs (the features below E_F) and RCBs (the features above E_F) with the period of the alternating appeared AA sites and DWs is observed. A noticeable trend is that both the DOS peaks of FBs and RCBs shift towards to E_F as the moiré triangle is getting smaller.

To further investigate the evolution of the FBs in TBG close to the first magic angle, we extract the dI/dV spectra on AA sites from 1.29° to 0.59° and plot them together (Fig. 2a). The corresponding twist angle of the AA site is denoted in each spectrum, which is determined as the average of the twist angles of the six moiré triangles surrounding the AA site. The colormap of Fig. 2a further highlights the evolution of the FBs (Fig. 2b). In general, as the twist angle gradually decreases from 1.29° to 0.59° , the left flat band (FB1) peak and the right flat band (FB2) peak gradually approach each other, and suddenly merge into one peak (FB3) between 0.78° and 0.74° . More importantly, near the magic angle, we can observe a clear spectral weight transfer from the peak of FB1 to the peak of FB2, giving rise to an extremely sharp FB2 peak and weak FB1 peak (see the region within the white dashed box). Such a spectral weight transfer leads to unequal integrals of spectral weight between the two FBs around the magic angle. This suggests correlation effects beyond the single-particle band theory or Hartree-Fock mean field theory (which would yield two FBs with approximately equal integrals of spectral weight), even if the FBs are fully filled.

More insights into the FBs' evolution are obtained by extracting the peak positions (Fig. 2c), peak heights (Fig. 2d), and peak widths (Fig. 2e) of the FB states from the dI/dV spectra (see details in Supplementary Material). The peak position of FB2 is fixed when it exists, while the peak position of FB1 fluctuates with the twist angle (Fig. 2c).

The energy separation between the two FBs peaks shows a slow decrease as the twist

angle changes from 1.29° to 0.95° (Fig. 2c), during which the corresponding strain is around 0.8% and almost unchanged (see the schematic arrows of strains in Fig. 2b and 1c, and more details are shown in Fig. S2). In contrast, as the twist angle is less than 0.8° , the energy separation decreases rapidly then merge together, and the corresponding strain dramatically decreases from 0.8% to 0. The observed energy separation trend here is consistent with the theoretical prediction³³ that the strain dominates the contribution to the energy separation of FBs.

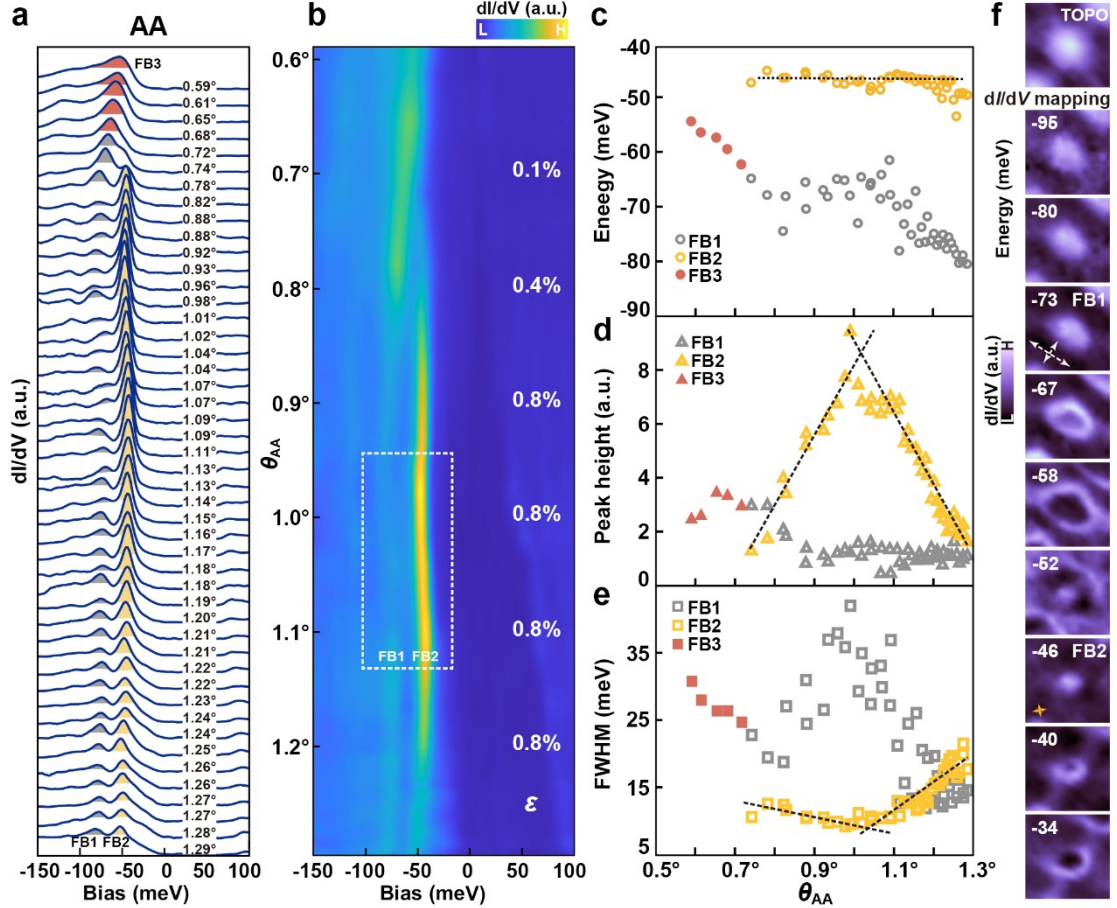


Fig. 2 | Twist angle dependent evolution of the flat bands on AA sites close to the first magic angle. **a**, Tunneling spectra on AA sites as a function of calculated twist angle θ_{AA} . For clarity, each curve has an equal offset. As θ_{AA} is greater than a critical value around 0.7° , the peaks of the two flat bands (FB1 and FB2) are well separated and are painted in grey and yellow, respectively. As θ_{AA} drops below the critical value, only one peak (FB3) can be recognized and is painted in red. Set point: $V_s = -200$ mV, $I_t = 200$ pA. **b**, Colormap of **a** to further visualize the peaks evolution. **c-e**, Energy, peak height and full width at half maxima (FWHM) of the FB states as a function of θ_{AA} . The black dashed lines denote the evolution trends of the three values. Spectral weight transfer from FB1 to FB2 occurs near the magic angle, corresponding to the enhanced (decreased) intensity of FB2 (FB1) peak in the white dashed box area in **b**. **f**, Topography and dI/dV map near AA29 site with the twist angle of 1.02° (15.4 nm \times 15.4 nm). The spatial distribution of density of states at the energies of FB1 and FB2 are both elongated, the anisotropic spatial distribution of the FBs is marked by the gray and yellow double-headed arrows. Set point: $V_s = -200$ mV, $I_t = 200$ pA.

The anomalous spectral weight transfer from FB1 to FB2 is further confirmed. In the angle range of 0.95° to 1.13° (marked by the white dashed box in Fig. 2b), the DOSs of FB2 are significantly enhanced and the peak height (width) of FB2 reaches a maximum (minimum) near the magic angle (Fig. 2d and e), representing the "flattening" behavior of the moiré band⁴³. While, in contrast, FB1 shows an opposite behavior and almost invisible. When the twist angle is smaller than 1.02° (see the crossing point of the guide lines in Fig. 2d and e), the heights of FB2 starts to decrease and FB1 gradually revives. With the partially filling of the FBs, the spectral weight redistribution of the FB peaks may correspond to the strongly correlated electronic interactions of FBs⁸. Our results demonstrate that, even with the full filling of the FBs, the interaction effect between the two FBs also need to be revisited, which may be strongly altered by the gradient of twist angle and strain.

Figure 2f shows STM topography and DOS maps of the AA site with the twist angle of 1.02° . The DOSs' spatial distribution of FB1 (-73 meV) and FB2 (-46 meV) are concentrated at the AA site center. FB2 is more localized, while FB1 has wider expansion. Off the FB1 (or FB2) energies, the elongated DOS spots in the AA site gradually protrude outward from the center, forming a ring-like feature⁴⁴. The spatial anisotropy of FB1 is more significant than that of FB2 (marked by double-headed arrows in Fig. 2f, and see Fig. S3 for comparison). The irregular shape of the spatial distribution of the electronic states of the FBs indicates additional symmetry breaking of AA site. Prior to the discussion of the symmetry breaking, it's highly worthwhile to take the RCB into consideration.

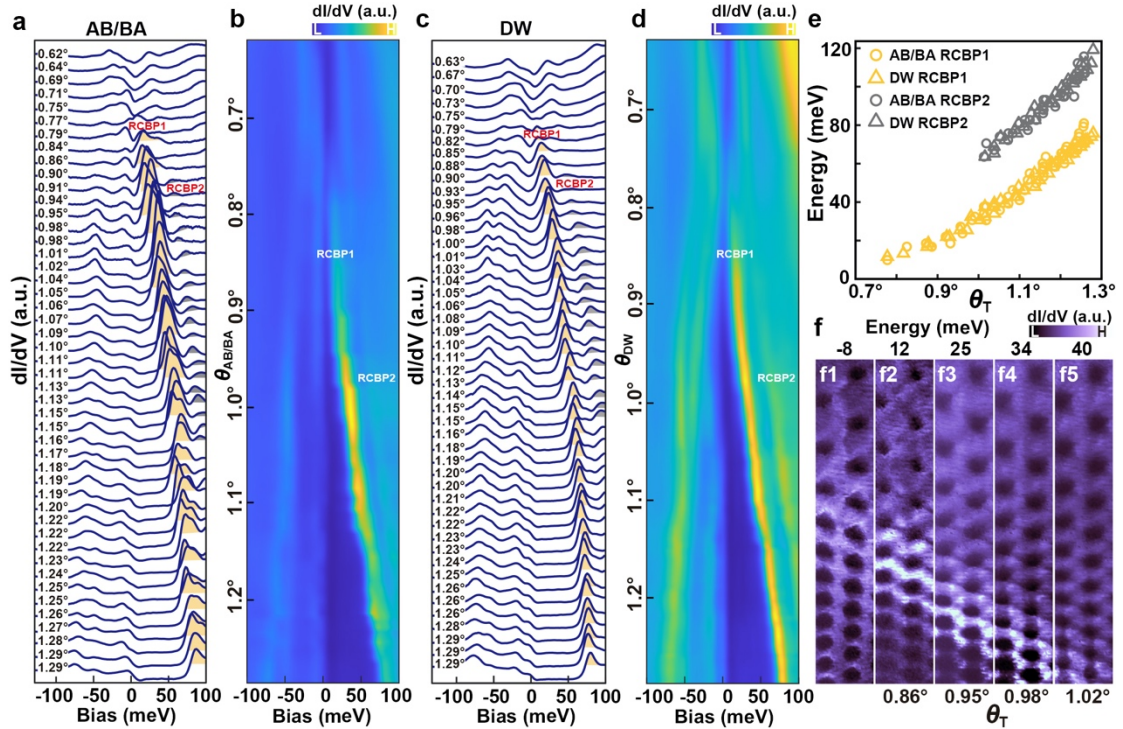


Fig. 3 | Twist angle dependent evolution of remote conduction band peaks on DWs and AB/BA domains. **a**, Tunneling spectra on AB/BA sites as a function of twist angle $\theta_{AB/BA}$. **b**, Corresponding colormap of **a**. **c**, Tunneling spectra on DW sites as a function of twist angle θ_{DW} . The first RCBP (RCBP1) and the second RCBP (RCBP2) are painted in yellow and gray, respectively. **d**, Colormap of **c**. **e**, The evolution of RCBP1 and RCBP2 on DW and AB/BA

sites with twist angle θ_T ($\theta_{AB/BA}$ or θ_{DW}). **f1-f5**, dI/dV maps taken at different RCBP1 energies ($32 \text{ nm} \times 170 \text{ nm}$). The brighter region in each map corresponds to the spatial distribution of the RCBP1 with specific energy, and the average twist angles of the brighter regions are shown below. Set point: **a, c, f**, $V_s = -200 \text{ mV}$, $I_t = 200 \text{ pA}$.

The remote conduction band peak (RCBP) is mainly located on AB/BA domains and DWs, where the FBs' contribution to DOSs no longer dominates. The dI/dV spectra on the center of AB/BA domains and DWs show the evolution of the first RCBP (RCBP1) and the second RCBP (RCBP2) as a function of twist angle (Fig. 3a-d). The twist angle of a DW is determined by the averaged twist angles of the two moiré triangles on both sides of the DW, and the twist angle of an AB/BA domain is calculated from the moiré triangle itself. The energy of RCBP shows a clean one-to-one relationship with the twist angle (Fig. 3e), but is insensitive to strain (see Fig. S4). With the angle-related RCBP1, we can highlight the TBG region with a specific twist angle in DOS maps by selecting a corresponding RCBP1 energy (Fig. 3f and see details in Fig. S5). Based on the highlighted moiré superlattices (with the identical twist angle) in each map, the direction of the twist angle gradient can also be easily determined.

Now we turn to the symmetry breaking of FBs on AA site. Figure 4a shows the topography of an area near the yellow box region. The corresponding dI/dV maps with different selected energies of RCBP1 highlight several line-shaped areas, and within each "line" the twist angle is identical (see the highlighted areas and the colored equiangular lines in Fig. 4b-d and Fig. S6). The DOS maps of FBs are elongated (Fig. 2f and Fig. S7), indicative of symmetry breaking. We attach double-headed arrows to denote the longest side direction of the DOS maps, showing the orientations and magnitudes of symmetry breaking of FB2 and FB1 (the yellow and grey arrows in Fig. 4e and f). Figure 4g integrates all the equiangular lines and arrows from Fig. 4b-f.

The twist angles in Fig. 4g are divided into 5 equal intervals and the corresponding equiangular lines are plotted in different colors (Fig. 4h). The arrows with various orientations are counted to their nearest equiangular line and plotted in Fig. 4h. The direction of twist angle gradient is perpendicular to the equiangular line from higher angle to lower angle (see the upper panel of Fig. 4h). The statistical result shows that the symmetry breaking direction of FB1 (the grey arrows) is locked with the equiangular line or the twist angle gradient (the middle panel of Fig. 4h). While the symmetry breaking directions of FB2 are less bounded with the angle gradient (the bottom panel of Fig. 4h). These results indicate that the symmetry breaking of FB1 is strongly related to the twist angle inhomogeneity and FB2 is less influenced than FB1. The relationship between the symmetry breaking of the FBs and the strain is unclear, and detailed discussions are shown in Fig. S8-S9.

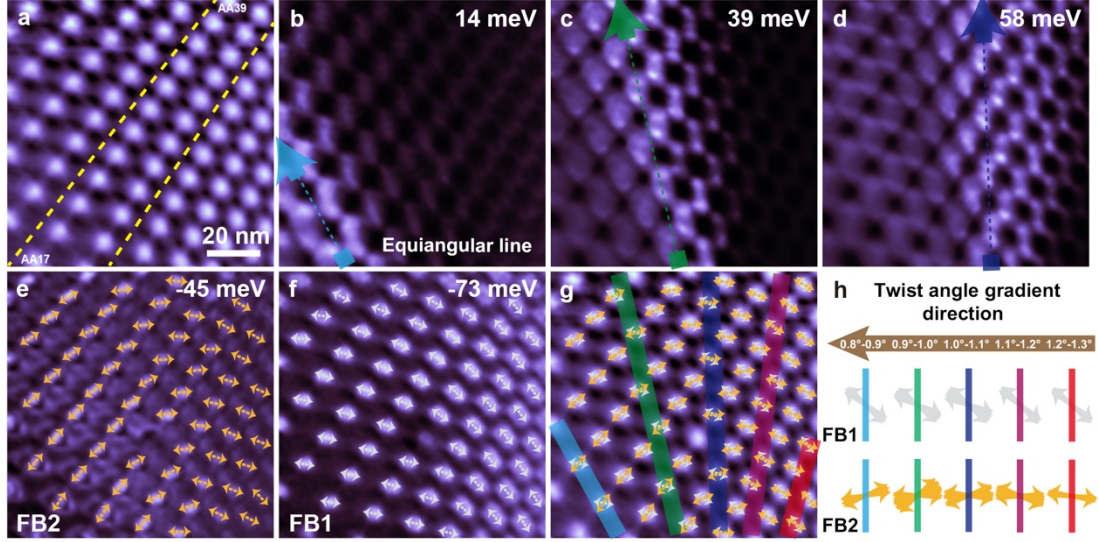


Fig. 4 | Symmetry breaking of flat bands on AA sites. **a**, Topography of the studied region (100 nm \times 100 nm), the yellow dashed lines and the AA numbers mark the relation with the yellow box region. **b-d**, dI/dV maps at the energies of RCBP1, which highlight the different equiangular lines on the region. The incomplete arrows mark the directions of the equiangular lines. **e-f**, dI/dV maps of the FB2 and FB1. The symmetry breaking directions of FB2 (FB1) on AA sites are denoted by yellow (grey) dashed double-head arrows. **g**, Topography integrates the equiangular lines and the symmetry breaking directions of FBs from **b-f**, and the equiangular lines are colored with wathet, green, blue, magenta and red, respectively. **h**, Statistical results of the symmetry breaking direction of FBs. The twist angles are divided into 5 equal intervals and displayed at the upper panel, and the brown arrow is the twist angle gradient direction. The colored lines are corresponding to the equiangular lines in **b-d** and **g**. The grey (yellow) double-head arrows are the relative symmetry breaking directions of FB1 (FB2) from **f(e)**. Set point: $V_s = -200$ mV, $I_t = 200$ pA.

Owing to the strain-induced inhomogeneity, we obtain continuous evolution of the electronic structures of the FBs and RCBs of TBG over a wide twist angle range from 0.32° to 1.29° . We emphasize on the following issues.

(1) We demonstrate that the electronic states of FBs and RCBs mainly locate on AA sites and AB/BA regions, respectively. Moreover, the spatial evolution of the FB peaks in the vicinity of the AA sites within a moiré triangle (Fig. 1e) gives rise to the observed ring-like DOS map around the AA sites (Fig. 2f), which may be related to the hybridization of the FBs with other bands.

(2) The energy of RCBP positively correlates with the twist angle (Fig. 3e), but is insensitive to strain. The RCBP can thus be an index for the twist angle in a TBG device.

(3) Many theoretical works used the Hartree-Fock approximation model to calculate the renormalization of the band structure of TBG at partial filling^{43, 45-47}. Here we demonstrate that, even with the fully occupied FBs, correlated interactions between the two FBs still persist, as evident from the spectral weight transfer, which calls for further theoretical investigation.

(4) The influences of the twist angle gradient on symmetry breaking of the FBs are

diverse. Regarding the FB1, its symmetry is fragile and can be easily broken by the angle gradient; its spatial anisotropy is large and has wide expansion in space. Regarding the FB2, its symmetry can resist the influences of the angle gradient; its anisotropy is weak and FB2 is localized at the AA site.

Reference

1. Bistritzer, R. & MacDonald, A.H. Moire bands in twisted double-layer graphene. *Proceedings of the National Academy of Sciences of the United States of America* **108**, 12233-12237 (2011).
2. Nam, N.N.T. & Koshino, M. Lattice relaxation and energy band modulation in twisted bilayer graphene. *Phys Rev B* **96**, 075311 (2017).
3. Andrei, E.Y. & MacDonald, A.H. Graphene bilayers with a twist. *Nat. Mater.* **19**, 1265-1275 (2020).
4. Cao, Y. et al. Correlated insulator behaviour at half-filling in magic-angle graphene superlattices. *Nature* **556**, 80-84 (2018).
5. Xie, Y.L. et al. Spectroscopic signatures of many-body correlations in magic-angle twisted bilayer graphene. *Nature* **572**, 101-105 (2019).
6. Wong, D.L. et al. Cascade of electronic transitions in magic-angle twisted bilayer graphene. *Nature* **582**, 198-202 (2020).
7. Kerelsky, A. et al. Maximized electron interactions at the magic angle in twisted bilayer graphene. *Nature* **572**, 95-100 (2019).
8. Jiang, Y.H. et al. Charge order and broken rotational symmetry in magic-angle twisted bilayer graphene. *Nature* **573**, 91-95 (2019).
9. Choi, Y. et al. Electronic correlations in twisted bilayer graphene near the magic angle. *Nature Physics* **15**, 1174-1180 (2019).
10. Cao, Y. et al. Unconventional superconductivity in magic-angle graphene superlattices. *Nature* **556**, 43-50 (2018).
11. Saito, Y., Ge, J., Watanabe, K., Taniguchi, T. & Young, A.F. Independent superconductors and correlated insulators in twisted bilayer graphene. *Nat. Phys.* **16**, 926-930 (2020).
12. Oh, M. et al. Evidence for unconventional superconductivity in twisted bilayer graphene. *Nature* **600**, 240-245 (2021).
13. Lu, X.B. et al. Superconductors, orbital magnets and correlated states in magic-angle bilayer graphene. *Nature* **574**, 653-657 (2019).
14. Yankowitz, M. et al. Tuning superconductivity in twisted bilayer graphene. *Science* **363**, 1059-1064 (2019).
15. Hao, Z.Y. et al. Electric field-tunable superconductivity in alternating-twist magic-angle trilayer graphene. *Science* **371**, 1133-1138 (2021).
16. Serlin, M. et al. Intrinsic quantized anomalous Hall effect in a moire heterostructure. *Science* **367**, 900-903 (2020).
17. Zhang, Y. et al. Correlation-induced valley splitting and orbital magnetism in a strain-induced zero-energy flatband in twisted bilayer graphene near the magic angle. *Phys Rev B* **102**, 081403 (2020).
18. Wu, S., Zhang, Z., Watanabe, K., Taniguchi, T. & Andrei, E.Y. Chern insulators, van

- Hove singularities and topological flat bands in magic-angle twisted bilayer graphene. *Nat. Mater.* **20**, 488-494 (2021).
19. Song, Z.D. et al. All Magic Angles in Twisted Bilayer Graphene are Topological. *Physical Review Letters* **123**, 036401 (2019).
 20. Saito, Y. et al. Hofstadter subband ferromagnetism and symmetry-broken Chern insulators in twisted bilayer graphene. *Nature Physics* **17**, 478-481 (2021).
 21. Sharpe, A.L. et al. Emergent ferromagnetism near three-quarters filling in twisted bilayer graphene. *Science* **365**, 605-608 (2019).
 22. Pierce, A.T. et al. Unconventional sequence of correlated Chern insulators in magic-angle twisted bilayer graphene. *Nature Physics* **17**, 1210-1215 (2021).
 23. Nuckolls, K.P. et al. Strongly correlated Chern insulators in magic-angle twisted bilayer graphene. *Nature* **588**, 610-615 (2020).
 24. Zhang, C.X. et al. Visualizing delocalized correlated electronic states in twisted double bilayer graphene. *Nature Communications* **12**, 2516 (2021).
 25. Yin, J.-X., Pan, S.H. & Zahid Hasan, M. Probing topological quantum matter with scanning tunnelling microscopy. *Nature Reviews Physics* **3**, 249-263 (2021).
 26. Yoo, H. et al. Atomic and electronic reconstruction at the van der Waals interface in twisted bilayer graphene. *Nature Materials* **18**, 448-453 (2019).
 27. Zondiner, U. et al. Cascade of phase transitions and Dirac revivals in magic-angle graphene. *Nature* **582**, 203-208 (2020).
 28. Lu, X. et al. Multiple flat bands and topological Hofstadter butterfly in twisted bilayer graphene close to the second magic angle. *Proceedings of the National Academy of Sciences* **118**, e2100006118 (2021).
 29. Uri, A. et al. Mapping the twist-angle disorder and Landau levels in magic-angle graphene. *Nature* **581**, 47-52 (2020).
 30. Wilson, J.H., Fu, Y., Das Sarma, S. & Pixley, J.H. Disorder in twisted bilayer graphene. *Physical Review Research* **2**, 023325 (2020).
 31. Yan, W. et al. Strain and curvature induced evolution of electronic band structures in twisted graphene bilayer. *Nat. Commun.* **4**, 2159 (2013).
 32. Lau, C.N., Bockrath, M.W., Mak, K.F. & Zhang, F. Reproducibility in the fabrication and physics of moiré materials. *Nature* **602**, 41-50 (2022).
 33. Bi, Z., Yuan, N.F.Q. & Fu, L. Designing flat bands by strain. *Phys Rev B* **100**, 035448 (2019).
 34. Mesple, F. et al. Heterostrain Determines Flat Bands in Magic-Angle Twisted Graphene Layers. *Physical Review Letters* **127**, 126405 (2021).
 35. Qiao, J.-B., Yin, L.-J. & He, L. Twisted graphene bilayer around the first magic angle engineered by heterostrain. *Phys Rev B* **98**, 235402 (2018).
 36. Shi, H. et al. Large-area, periodic, and tunable intrinsic pseudo-magnetic fields in low-angle twisted bilayer graphene. *Nature Communications* **11**, 371 (2020).
 37. Kazmierczak, N.P. et al. Strain fields in twisted bilayer graphene. *Nature Materials* **20**, 956-963 (2021).
 38. Miao, F., Liang, S.J. & Cheng, B. Straintronics with van der Waals materials. *Npj Quantum Mater* **6**, 59 (2021).
 39. Brihuega, I. et al. Unraveling the intrinsic and robust nature of van Hove singularities

- in twisted bilayer graphene by scanning tunneling microscopy and theoretical analysis. *Phys. Rev. Lett.* **109**, 196802 (2012).
40. Wang, W.X. et al. Scanning tunneling microscopy and spectroscopy of finite-size twisted bilayer graphene. *Phys Rev B* **96**, 115434 (2017).
 41. Wong, D. et al. Local spectroscopy of moire-induced electronic structure in gate-tunable twisted bilayer graphene. *Phys Rev B* **92**, 155409 (2015).
 42. Li, S.Y. et al. Splitting of Van Hove singularities in slightly twisted bilayer graphene. *Phys Rev B* **96**, 155416 (2017).
 43. Lewandowski, C., Nadj-Perge, S. & Chowdhury, D. Does filling-dependent band renormalization aid pairing in twisted bilayer graphene? *Npj Quantum Mater* **6**, 82 (2021).
 44. Liu, Y.W. et al. Tunable Lattice Reconstruction, Triangular Network of Chiral One-Dimensional States, and Bandwidth of Flat Bands in Magic Angle Twisted Bilayer Graphene. *Phys Rev Lett* **125**, 236102 (2020).
 45. Rademaker, L., Abanin, D.A. & Mellado, P. Charge smoothening and band flattening due to Hartree corrections in twisted bilayer graphene. *Phys Rev B* **100**, 205114 (2019).
 46. Cea, T., Walet, N.R. & Guinea, F. Electronic band structure and pinning of Fermi energy to Van Hove singularities in twisted bilayer graphene: A self-consistent approach. *Phys Rev B* **100**, 205113 (2019).
 47. Goodwin, Z.A.H., Vitale, V., Liang, X., Mostofi, A.A. & Lischner, J. Hartree theory calculations of quasiparticle properties in twisted bilayer graphene. *Electron Struct* **2**, 034001 (2020).

Methods

STM measurements.

Our experiments were carried out on an ultrahigh-vacuum commercial STM system (Unisoku) that operated on a constant base temperature of 4.2 K with optical microscope observation. The base pressure of the system is 1.0×10^{-10} Torr. The TBG device were degassed at 170°C under ultra-high vacuum before transferring into the STM. The STS data were obtained by a standard lock-in method that applied an additional small a.c. voltage with a frequency of 973.0Hz. The dI/dV spectra were collected by disrupting the feedback loop and sweeping the d.c. bias voltage.

TBG device.

The twisted bilayer graphene samples were prepared by using the clean dry transfer method. First, monolayer graphene was exfoliated onto a clean SiO₂/Si substrate. A BN flake attached to Polydimethylsiloxane (PDMS) stamp was then positioned above the monolayer graphene under an optical microscope. Half of the monolayer graphene was picked up by the BN on PDMS, forming PDMS/BN/Graphene structure. Then the other half of the graphene was rotated to the desired twist angle and picked up by the PDMS/BN/Graphene heterostructure. Subsequently, the PDMS/BN/tBLG structure was flipped over, and the BN/tBLG sample was picked up by another PDMS stamp and then transferred onto a gold-coated substrate. The cleanness and quality of the tBLG sample are critical for obtaining high-quality STM data. Finally, one piece of graphite was used to connect the graphene and the gold-coated substrate to ensure good electrical conductivity during STM measurements.

Data availability.

The data that support the findings of this study are included in this article and its supplementary information file and are available from the corresponding author upon reasonable request.

Acknowledgements

J. Yu, G. Jia and Q. Li contributed equally to this work. We thank Z. Song and S. Yuan for helpful discussions. The research was supported by the National Science Foundation of China (Grants No. 92365201, No. 51788104, No. 11427903, and No. 12234011) and the Ministry of Science and Technology of China (Grant No. 2022YFA1403100 and No. 2021YFA1400100), the Initiative Research Projects of Tsinghua University (No. 20211080075), and the Beijing Advanced Innovation Center for Future Chip (ICFC). B. L. is supported by the National Science Foundation under award DMR-2141966, and the National Science Foundation through Princeton University's Materials Research Science and Engineering Center DMR-2011750.

Author contributions

W.L., S.Z. and Q.-K.X. conceived and supervised the research project. J.Y., K.X., Z.H. and Y.G. performed the STM experiments. Q.L., H.Z. and S.Z. prepared the TBG device. W.L.,

J.Y., G.J., Y.W., Y.J., B.L. and P.T. analyzed the data. W.L., J.Y., G.J. and Y.W. wrote the manuscript with input from all other authors.

Competing interests

The authors declare no competing interests.